Early stages of scale formation during oxidation of γ/γ′ strengthened single crystal ternary Co-base superalloy at 900 °C

Martin Weiser[a], Yolita M. Eggeler[b], Erdmann Spiecker[b], Sannakaisa Virtanen[a,*]

[a] *Institute for Surface Science and Corrosion, Friedrich-Alexander-Universität Erlangen-Nürnberg (FAU), Martensstr. 7, 91058 Erlangen, Germany*
[b] *Institute of Micro- and Nanostructure Research and Center for Nanoanalysis and Electron Microscopy (CENEM), Friedrich-Alexander-Universität Erlangen-Nürnberg (FAU), Cauerstr. 6, 91058 Erlangen, Germany*

A B S T R A C T

A study on the individual role of γ and γ′-phase during the scale formation on Co-9Al-9W (at.%) at 900 °C was conducted. High-accuracy thermogravimetric analysis was used to locate changes in the kinetics of scale growth. Compositions of three separated layers within the scale have been elucidated in detail. The results demonstrate the substantial impact of the two-phase microstructure on the initiation of oxidation for the appearance of the scale. Examination of STEM-EDX elemental mappings of the internal oxidation front during the early stages of scale growth can explain the origin of isolated Al_2O_3 precipitates instead of a closed protective layer.

1. Introduction

Since the discovery of a stable $L1_2$ phase in the ternary Co-Al-W system by Sato et al. in 2006 [1], the investigation of this new class of high temperature material has substantially expanded. The microstructure of these Co-base superalloys, cuboidal γ′ precipitates coherently embedded in a γ matrix, is similar to those of well-known Ni-base superalloys [2]. In recent years mechanical properties, such as creep resistance and yield strength at elevated temperature, could be improved by widening the range of considered alloying elements [3–6]. Nevertheless, the oxidation properties above 800 °C remained relatively poor. Extensive studies on the oxidation behaviour of Co-base superalloys between 800 and 900 °C were conducted since 2010 [7–12]. Hardly any of the investigated alloy compositions based on the ternary system showed a continuous, protective Al_2O_3-layer after oxidation for up to 500 h at 900 °C [8,11]. Interestingly, however, growth of a protective layer on Cr-free Co-based alloys during the oxidation in laboratory air at 800 °C could be demonstrated [9].

The above described oxidation behaviour stands in contrast to that of Ni-base superalloys already in use for high temperature application over decades. In oxidation resistant high temperature superalloys an advantageous balance between the progress of internal oxidation and diffusion velocity of alloying elements, such as Al or Cr, results in the formation of a protective Cr_2O_3 or Al_2O_3-layer after a relative short duration of exposure at 900 °C and above [13,14]. Due to the consumption of Al, the region below the protective oxide layer is depleted in γ′. Driven by high diffusion velocities of alloying elements, this

depletion is particularly pronounced for oxidation at elevated temperatures. Several studies on the role of γ′ phase on the formation of protective oxides in fourth generation Ni-base superalloys at 700 °C can be found in literature [15,16]. *In situ* oxidation experiments of a second generation Ni-base superalloy in a TEM were conducted to learn more about the oxygen diffusion paths at 850 °C [17].

During high temperature oxidation of Al-containing alloys, the formation of transient oxides is another interesting phenomenon. Even though only few groups addressed these questions, the potential for analytical TEM investigations to provide new microstructural insights in the reaction mechanisms during the early stages of scale formation was already demonstrated [18,19]. The long transient phase as well as the absence of a distinct γ′ depleted zone below the internal oxidation front (IOF) makes ternary Co-base superalloys an outstanding model system to investigate transient oxidation processes as well as the role of a two-phase microstructure on the progress of scale formation at high temperatures. Elucidation and understanding of elementary oxidation mechanisms can be an essential contribution in the community to find more oxidation resistant composition for this new class of alloys.

In the present work, classical experimental techniques such as thermogravimetry and subsequent evaluation of cross-sections are combined with high-resolution analytical scanning transmission electron microscopy (STEM). Elemental mappings of relevant regions in the complex multilayered oxide scale are attributed to changes measured in the oxidation kinetics. The ternary composition reported by Sato et al. [1] was chosen as a model system to gain detailed insights in elementary mechanisms occurring during oxidation in synthetic air at 900 °C.

Table 1
Chemical composition in atom percent of the investigated ternary Co-base superalloy.

Element	Co	Al	W
at.%	Bal.	9.6	9.0

2. Experimental procedures

2.1. Materials

A rod-shaped single-crystalline ternary Co-base superalloy with a nominal composition of Co-9Al-9W was casted in a Bridgman invest-ment casting facility by a project in the framework of the collaborative research center SFB-TR103 at the Institute of Metals Science and Technology (WTM, University of Erlangen-Nürnberg (FAU), Germany). To determine the chemical composition after heat treatment part of the alloy was dissolved and subsequently investigated by ICP-OES. Results are given in Table 1.

The heat treatment consisted of a 12 h homogenisation step at 1300 °C followed by a 200 h aging step at 900 °C. Discs with approxi-mately 0.8 mm height and 11 mm diameter were cut from the rod. Subsequently all samples were ground and polished down to 1 μm surface finish.

2.2. Isothermal oxidation

Isothermal oxidation experiments were conducted in a Setaram Evolution 1650 thermogravimetric analyser under constant gas flow of 20 cm³ min⁻¹. Prior to oxidation, the atmosphere inside the device was changed to Ar. After reaching the target temperature of 900 °C, the chamber was evacuated and subsequently filled with dry synthetic air (80%N_2 20%O_2). Several oxidation experiments with a maximum duration of 100 h were carried out. Prior to further metallographic preparation, the oxidised samples were protected by an electro-chemically deposited Ni-layer.

2.3. Electron microscopy

Samples were cut approximately in the middle. A representative region along the cut edge was polished with a Hitachi IM4000 ion milling system. Morphologies of cross-sections were subsequently in-vestigated in a scanning electron microscope (Hitachi FE-SEM S-4800). Distances were directly determined from the backscattered SEM mi-crographs with the imaging software ImageJ.

The preparation of the oxide layers as TEM samples was rather complex, due to the brittleness of the oxide layer itself. Two small pieces of the oxidised bulk sample were extracted along the ⟨100⟩ di-rection, using a wire saw. On top of the oxidised layer, a slice of su-peralloy base material was glued to protect the scale during the me-chanical preparation. The whole stack was clamped into a Titanium TEM sample plate carrier for subsequent one-sided grinding and pol-ishing. After reaching a common height with the plate carrier, a wedge grinding and polishing method (wedge angle of 5–7°) was applied to the opposite side. By then, the scale on tip of the sample had a thickness of about 20 μm. The final thinning was performed in different steps by ion milling. In the last step an acceleration voltage of 1 kV at 5° was used for 30 min to reach electron transparency.

Annular dark field scanning TEM (ADF-STEM) was performed on a double-aberration-corrected Titan Themis[3] 300 operating at an accel-eration voltage of 300 kV. In order to reveal the different oxides and phases, ADF-STEM was performed under conditions of *Z*-contrast using a small camera length of 115 mm. The high-resolution STEM-EDX mappings at 300 kV were carried out using a Super-X detector in-corporating the Bruker ChemiSTEM™ system. The Super-X detector comprises four silicon drift detectors (SDD) symmetrically placed
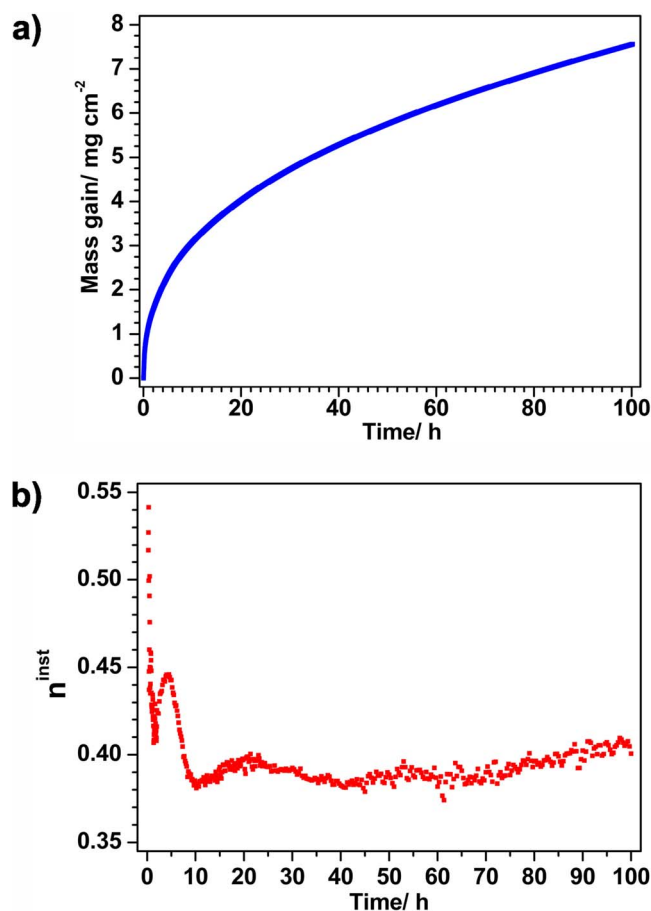
Fig. 1. (a) Mass gain of Co-9Al-9W at 900 °C during 100 h oxidation and (b) in-stantaneous time exponent n^{inst} for the duration of exposure.

around the optical axis, close to the sample area. All four signals are combined into one spectrum to improve the collection efficiency. More details explaining this system can be found in the literature [20–22].

Part of the EDX results are shown as colour coded element dis-tribution maps. For each investigated sample, mappings of the four relevant elements (Co, Al, W and O) are combined to one figure. Due to varying maximum concentrations, the colour coding is individually adjusted, with dark blue representing a low and red a high amount (at. %) of the corresponding element.

3. Results

3.1. Mass gain and multilayered scale growth at 900 °C

Mass gain of the ternary Co-base superalloy was continuously measured during 100 h isothermal oxidation in artificial air at 900 °C. Results are given in Fig. 1a. Prevailing kinetics are subjected to a first examination. A power rate law for mass gain was assumed for the whole duration of the oxidation experiment to draw first conclusions.

$$\Delta m = kt^n \tag{1}$$

The instantaneous time exponent n^{inst} is equal to the deviation of the double-logarithmic plot of mass gain over time. To reduce the noise, increments between the considered data points are increased with on-going progress of oxidation. The instantaneous time exponent is plotted for the whole range of performed oxidation experiments in Fig. 1b.

As noted by several authors, interpretation of instantaneous time exponents is not always straightforward. Nevertheless, this way of treating kinetic data can help to locate and isolate changes in the overall kinetics of the scale growth reactions. Scale growth processes at
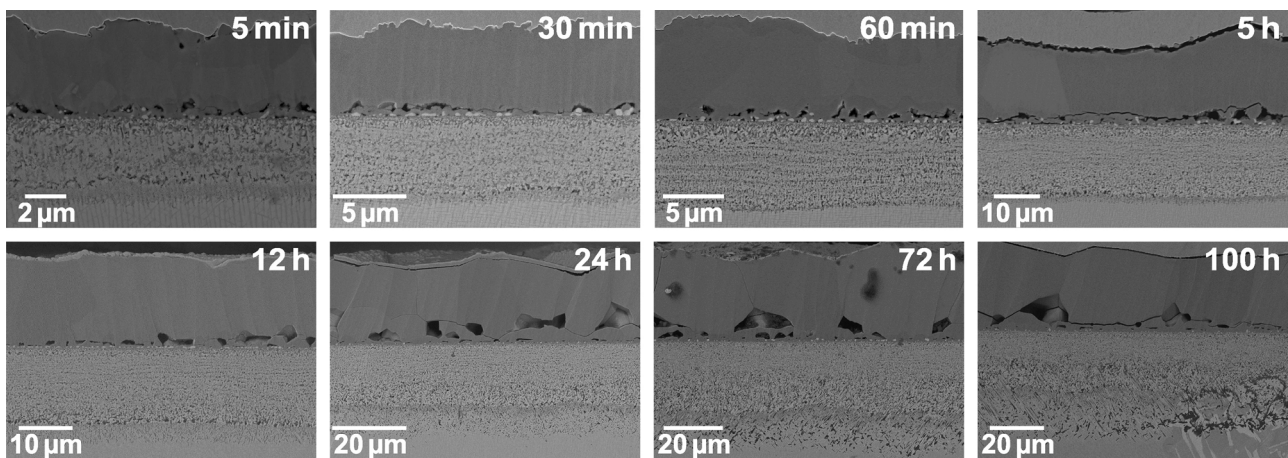
Fig. 2. Backscattered SEM micrographs of multilayered scales on Co-9Al-9W after different duration of exposure at 900 °C.

900 °C are known to be diffusion controlled. During the first 12 h after the onset of scale formation, the strong decrease of n^{inst} reveals a fast transition to slower oxidation kinetics. Anions and cations have to diffuse through the scale. Therefore, the overall composition and more specifically the portion of individually formed oxide phases within the scale are of pivotal importance for the growth kinetics [23]. After this initial period the change in oxidation kinetics gets less pronounced. A local maximum around 24 h and a moderate but steady increase of n^{inst} after 55 h can be identified.

Figs. 2 and 3 show a series of BSE images taken from cross-sections of multilayered scales grown for different times. After a sufficiently long duration of oxidation three individual layers can be clearly distinguished. In the following these layers are referred to as d_1, d_2 and d_3. Fig. 3 exemplarily shows the three layers of the scale grown during 100 h oxidation. Below the outer oxide layer d_1 the inner oxidation zone starts. The inner oxidation zone is distinguished into two separate regions d_2 and d_3. The inner oxidation layer (d_2) is a fully oxidised layer, where various oxides phases are present alongside each other. This layer is followed by d_3, which is a region of small (Al_2O_3) precipitates in unoxidised γ matrix. Compositions of each of the mentioned

layers is addressed at a later stage of this work. Strictly speaking d_3 is present from the onset of internal scale formation. However, it is not possible to clearly distinguish it from d_2 by SEM before 5 h of oxidation. The size of the precipitates is depending on the progress of oxidation. The formation of larger Al_2O_3 precipitates is accompanied by depletion of Al in the region enclosing the IOF. In ternary Co-base superalloys this Al depletion leads to the formation of the intermetallic DO_{19} phase (χ-Co_3W) [9,11]. First traces of this phase can already be observed after 12 h of oxidation (compare Fig. 3). After sufficiently long oxidation times (> 24 h) this new phase also forms further below the IOF. The well-known phase transformation does not contribute to the measured mass gain and presumably has only negligible effect on the diffusion of alloying elements. Therefore, it is not considered to be part of the scale.

A certain degree of porosity can be seen throughout the scale. Since the preparation of cross-sections is inevitable connected with mechanical forces, especially during cutting, some porosity might simply be caused by removal of material during preparation. The same is true for horizontally spread cracks, for example in Fig. 3 after 24 h exposure. Nevertheless pores and microchannels are known to form during the oxidation of Ni and Co alloys. Existing models describe the formation of
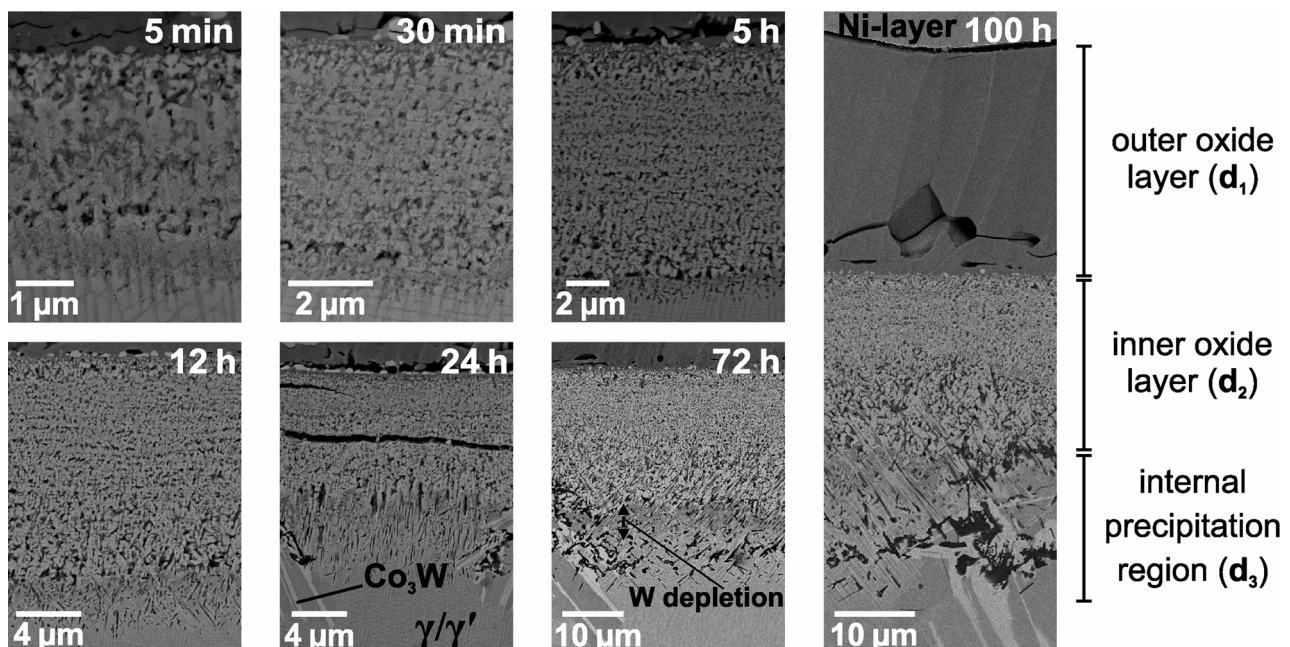

Fig. 3. Enlarged backscattered SEM micrographs showing the evolution of the inner oxidation layer with increasing time of exposure at 900 °C. The three distinguished layers are highlighted on a scale after 100 h oxidation (right).
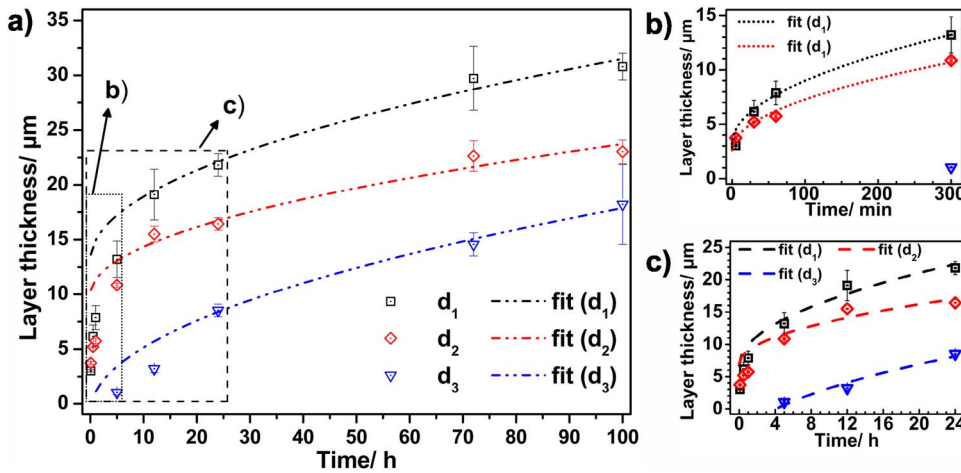
Fig. 4. Increase of layer thicknesses as function of oxidation time. Values were determined from representative SEM micrographs; (a) complete range of measured values with local fits (– ·) between [24 h; 100 h]; (b) layer thickness till 300 min exposure with local fits (···) between [5 min; 300 min]; (c) layer thickness till 24 h exposure with local fits (– –) between [5 h; 24 h].

voids mainly by the accumulation of vacancies due to fast diffusion of metal [24–26]. With ongoing metal transport even the formation of microchannels in the outer oxide layer is possible. The coarsening and spreading of rather large pores with ongoing oxidation in d_1 might be an indication, that such microchannels have already been formed in the investigated system.

Fig. 4 shows the evolution of the three individual layers over time. The (mean) thickness of each layer was calculated from five separated measurements on representative spots of the investigated cross-sections. The results are plotted with the standard deviation as error bars. Following the suggestions from Pieraggi [27] for oxidation reaction with fast initial kinetics, a $\Delta X - t^{1/2}$ dependency (compare Eq. (2)) was chosen to fit distinct intervals of the overall layer growth.

$$X = k_p^{sqr} \cdot \sqrt{t} \tag{2}$$

As stated, diffusion controlled growth of each individual oxide layer is assumed. In spite of this assumption it is not possible to fit the whole range of data points with sufficiently high accuracy for an individual layer by the simple Wagner dependency (Eq. (2)) given above (compare Fig. 4).

Instead, three individual local fits, each only taking data from an individual time window into account, were conducted. Measured values could be fitted with a reasonable accuracy in three time intervals. The k_p^{sqr} values are valid in a finite period during exposure. Results are summarised in Table 2. All fitted curves underlying the calculations of k_p^{sqr} are shown as lines in Fig. 4. For reasons of clarity, fits for times smaller than 24 h are shown as separate graphs (Fig. 4b and c). It can be seen in Fig. 4b that the conducted fit is already valid during the first 5 h of oxidation. Therefore, the initial assumption of diffusion controlled growth during the whole duration of exposure is confirmed by the measured and fitted data of layer thicknesses.

The decrease of parabolic rate constants k_p^{sqr} of the distinct layers during the early stages of oxidation is comparable to the substantial decay of n^{inst} in the first 12 h of scale formation (compare Fig. 1). All calculated k_p^{sqr} values decrease with ongoing isothermal exposure. The relative decrease of k_p^{sqr} values from each individual layer does not

follow one overall dependency. After considerable growth of d_3 within the inner oxidation zone, the parabolic rate constant for the internal precipitation zone d_3 drops by over 40%. Between 5 and 100 h, the k_p^{sqr} values undergo significantly slower changes. As already mentioned, a zone of Al-rich oxide precipitates embedded in an unoxidised matrix at the IOF starts to develop in samples oxidised for more than 1 h. At this stage it is difficult to already present a universal explanation for all processes taking place. Mass transport occurs across three differently composed layers, most probably in opposite directions. In the following, the focus is set on the IOF, the most essential region to understand the processes leading to the growth of protective layers. A transformation from internal to external scale growth is only possible if the counter current fluxes of alloying elements and opposed flux of oxygen at the IOF are balanced [28].

3.2. Nature of formed oxides

Especially during the transient stages of oxidation, the IOF progresses fast and forms various oxides simultaneously. To unravel this complex situation, information on every oxide included in the scale, is needed. Therefore, a XRD pattern was recorded from a sample after 72 h of isothermal exposure (Fig. 5). The peaks could be assigned mainly to contribution of the outer oxide layer d_1. Despite the substantial thickness of the outer oxide layer minor contributions might also be assigned to phases present in the inner oxide layer d_2. Peak
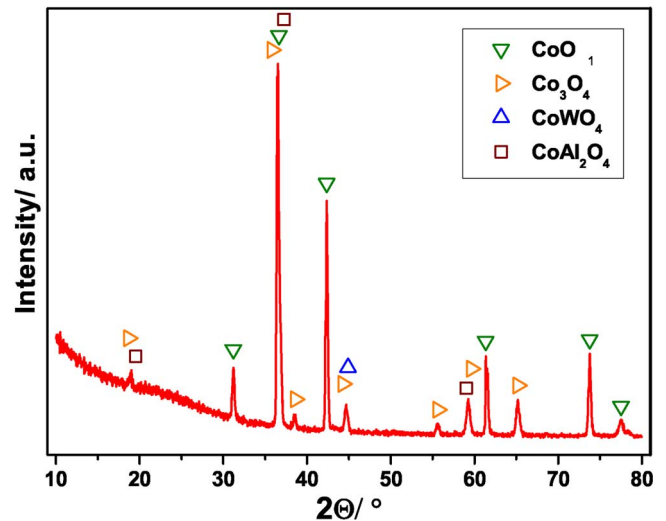
Table 2
Comparison of parabolic rate constants ($\frac{\mu m}{\sqrt{min}}$) for individual layer growth at 900 °C from curve fitting (Fig. 4).

Fit interval	k_p^{sqr} ($\frac{\mu m}{\sqrt{min}}$)		
	d_1	d_2	d_3
[5 min; 300 min]	0.578	0.466	
[5 h; 24 h]	0.413	0.265	0.366
[24 h; 100 h]	0.237	0.177	0.240

Fig. 5. XRD pattern of oxidised (72 h at 900 °C) Co-9Al-9W superalloy. Contributions of individual oxides are marked.
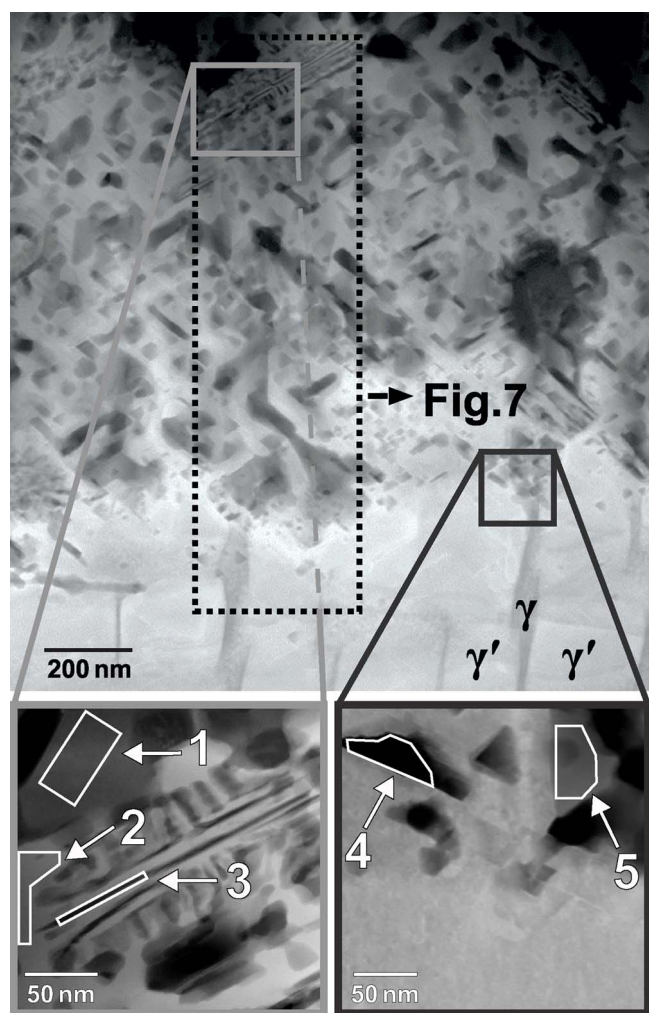
Fig. 6. STEM HAADF micrograph reveals a greater part of d_2 after 30 min. The two magnified areas on the right were analysed by STEM-EDX and the compositions of the numbered regions are given in Table 3.

Table 3
Composition (in at.%) extracted from STEM-EDX maps of representative regions included in d_2 (compare Fig. 6).

Map	Co	Al	W	O	Oxide
1	47.93	0.95	0.08	51.04	CoO
2	17.76	0.93	18.24	63.07	$CoWO_4$
3	18.34	21.09	3.68	56.90	$CoAl_2O_4$
4	1.38	37.23	0.32	61.06	Al_2O_3
5	18.12	2.74	18.31	60.83	$CoWO_4$

positions of potential contributions from further compounds, namely $CoWO_4$ and $CoAl_2O_4$ are also included in Fig. 5. As already stated in the literature, the outer oxide layer grown on Co-base superalloys at 900 °C consists of CoO and Co_3O_4 [9,10]. These experimental findings are also in good agreement with thermodynamic calculations on the layering of scales grown on ternary Co-base superalloys [29]. In combination with the XRD pattern in Fig. 5, the composition of this layer is sufficiently specified. All alloying elements are known to be present in the inner oxidation zone (compare [9,10]). Due to its high degree of complexity, detailed studies on the composition of the inner oxide layer (d_2) are not available in literature. A more detailed characterisation of the elemental distribution in the inner oxidation layer (d_2) helps to understand the mechanisms during the first transient stages of oxidation. Fig. 6 shows a HAADF STEM overview image of a section covering the greater

part of d_2 after 30 min oxidation. Notwithstanding the high complexity of this area, different oxides can already be clearly distinguished by the *Z*-contrast of the image. To locate the oxide phases detected by XRD within d_2, compositions were extracted from STEM-EDX maps of five representative regions within the inner oxide layer (see Fig. 6). The results are summarised in Table 3.

In Fig. 6 a change of morphology within d_2 is clearly apparent. Two regions, from the top including fine, lamellar structures and one close to the IOF including newly formed oxides were chosen for closer analysis. The upper magnified region in Fig. 6 shows lamellar $CoAl_2O_4$ spinels (map 3). Presence of $CoAl_2O_4$ in internal scales grown during cyclic oxidation at 800 °C on ternary Co-base superalloys has already been reported in literature [11]. Adjacent to the Al containing spinel, $CoWO_4$ (map 2) and CoO (map 1) can be found. The combination of these three oxides can be encountered repeatedly with similar morphology throughout the upper section of d_2. Closer to the IOF, $CoAl_2O_4$ has not been formed (yet). Two more analyses of oxides grown in a γ channel (maps 4 and 5 in Fig. 6) at the IOF were taken. These precipitates are Al_2O_3 and $CoWO_4$, respectively. An elemental mapping across d_2 sustains the location of the identified oxides. Both, the HAADF STEM micrograph (Fig. 6) as well as the elemental mapping (Fig. 7) show coarsening in the morphology of d_2 from top to bottom. A closer look at the elemental map reveals that this coarsening is particularly pronounced for Al containing phases. This finding gives a close insight in the ratio of counter current diffusion fluxes which are addressed at a later section of this work.

3.3. Evolution of the internal oxidation front

Changes appearing in the IOF between the onset of scale formation and 5 h of oxidation are of particular interest to reveal significant differences in the prevailing mechanisms. With longer duration, the amount of available oxygen per interval Δt decreases steadily. This is accompanied with an unaltered high availability of Al from the unoxidised alloy below the IOF. Already Wagner [30] considered mass balances in the IOF for the most essential processes to explain the transition from internal to external oxide layers. As mentioned above, the γ′ phase is only stable in a narrow compositional range. Therefore, the two-phase microstructure close to the IOF offers the unique opportunity to draw qualitative conclusions on relative diffusion velocities of both alloying elements. For this purpose, elemental distributions from the region enclosing the IOF were acquired using quantitative STEM-EDX. Two dimensional element distribution maps were taken after 5, 30 and 300 min. The results are shown in Figs. 8–10.

It is known from literature that W partitions strongly in the γ′ phase whereas the distribution of Al occurs homogeneously across the alloy [31]. These findings help to estimate the diffusion of W and Al in the course of oxidation time. If the two-phase microstructure becomes visible in the Al map, it is a clear indication for significant diffusion/depletion of Al in one of the two phases. The contrary applies for the distribution of W.

In Fig. 8, most of the image displays one unoxidised γ channel surrounded by γ′ cubes. The IOF is located at the top of the image. After 5 min oxidation, Al_2O_3 and $CoWO_4$ grow adjacently on the interface between scale and alloy. Precipitation of Al_2O_3 appears first in the γ channel (compare white arrow in Fig. 8). The region surrounding the newly formed small precipitate is depleted in Al. A minor Al gradient (marked in Fig. 8) extends in direction of the alloy along the γ channel, whereas the γ′ precipitates reveal an unaltered Al concentration.

The mappings in Fig. 9 cover a larger area of oxide above the IOF. After 30 min of oxidation the distribution of elements is mostly comparable to the distribution after 5 min. Due to the progress of the oxidation front, the Al gradient inside the γ channels is more pronounced. Compared to the situation after 5 min oxidation, a substantial change in the ratio of diffusion fluxes occurred. The diffusion velocity of Al can be expected to be nearly constant, while the progress of the oxidation front
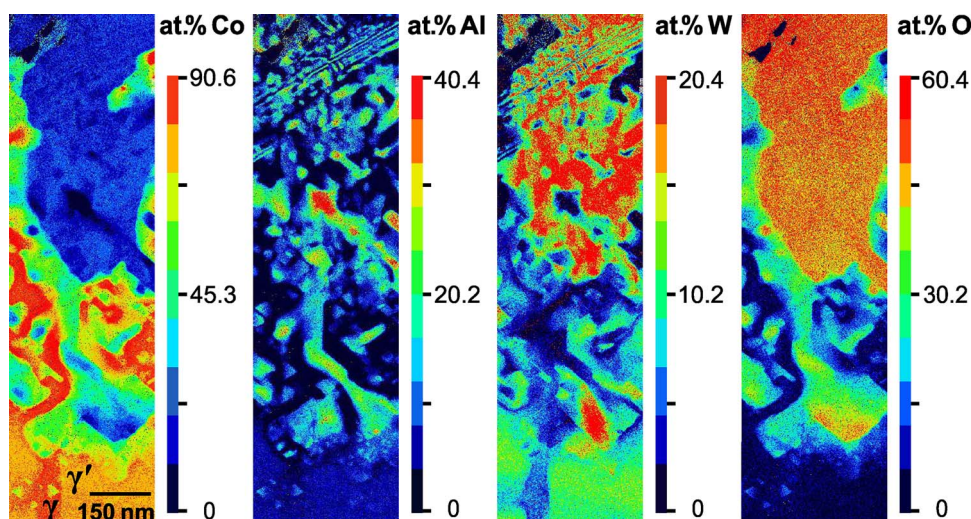
Fig. 7. Colour coded element distribution maps (in at.%) for, Co, Al, W and O (left to right) showing the boxed part of the inner oxide layer (Fig. 6) after 30 min exposure.

slows down continuously, since the diffusion path for oxygen gets longer. Insular growth of Al_2O_3 and $CoWO_4$ (see arrows in the Al and W map of Fig. 9) can be seen in the inner oxidation layer. In the γ channels an accumulation of Al is visible. It is worth noting that several traces of Al_2O_3 can be found in close proximity. This could be an indication for a high precipitation rate of Al_2O_3 within the matrix phase.

The mapping in Fig. 10 shows the IOF after 5 h. In contrast to the interfaces after shorter times, the third layer, d_3, is already developed to a larger extent. The Al_2O_3 precipitates show a rod-like shape, in some cases longer than 200 nm. The diameter remains relatively constant over the length of the precipitate. In the Al mapping, depletion along γ channels is clearly visible in the bottom left and right region of the image. In the W mapping the outline of a γ′ cube below the IOF, marked with a white ellipse, is still recognisable. In the corresponding regions of the Co and Al mapping the elemental concentrations are lower than in unaltered γ′ cubes. This finding indicates that after 5 h the depletion of Al expands from exclusively along the γ channels (5 and 30 min) to both phases. The top of the W map shows first traces of W depletion around the formed oxides.

4. Discussion

4.1. Transient oxidation stages

The transient oxidation behaviour of a ternary Co-9Al-9W superalloy was investigated for up to 100 h in detail. Besides the chemical composition of the inner oxide layer, another focus was set on the transient stages during the first 12 h of oxidation. With the help of high-resolution STEM it is possible to discuss the mechanisms which lead to the disadvantageous oxidation properties of Co-base superalloys at

temperatures of 900 °C (and above).

A series of schematic drawings, representing the situation on the IOF are shown in Fig. 11. The considered time range lies between 5 min and 12 h. For reasons of simplicity, only Al depletion is shown as a gradient (from dark (more Al) to bright (less Al)) in the gray value of the γ phase. It is reasonable to distinguish two oxidation fronts. The IOF classically describes the region of the deepest penetration of oxide. The IOF is followed by a second oxidation front, the interface between inner oxidation layer (d_2) and internal precipitation region (d_3). Due to the relatively fast penetration of oxygen through the scale during the whole duration of exposure, oxides are formed rapidly at the IOF. A more detailed consideration on the role of different phases was gained with help of STEM-EDX mappings. The most stable phase present in the scale is Al_2O_3. After short durations precipitations of Al_2O_3 are solely found in the γ phase. The existence of Al_2O_3 can be considered sufficiently certain referring to all elemental mappings. Due to the high thermo-dynamical stability of Al_2O_3 the least amount of oxygen is sufficient to form this phase. Therefore it is the first phase to be established at the IOF. First principal calculation on scales grown on quaternary Co-base superalloys performed by Stewart et al. [12] assessed the stability of potential oxide species. In the investigated system, Al_2O_3 is the most stable species, followed by $CoAl_2O_4$ and then $CoWO_4$. CoO is the least stable oxide formed on the outer layer. The investigated oxide compositions (Fig. 6) demonstrated the presence of CoO in the inner oxide layer as well. The EDX mappings after 5 and 30 min indicate that the first oxide species form in the γ channels. At this early stage of oxidation ($t < t_3$), after all Al from a certain volume increment is consumed, enough oxygen is left to form less stable oxides. These oxides are $CoWO_4$ and later CoO which can be found in close proximity of Al_2O_3 in the former γ channels. Due to the increase in scale thickness with longer
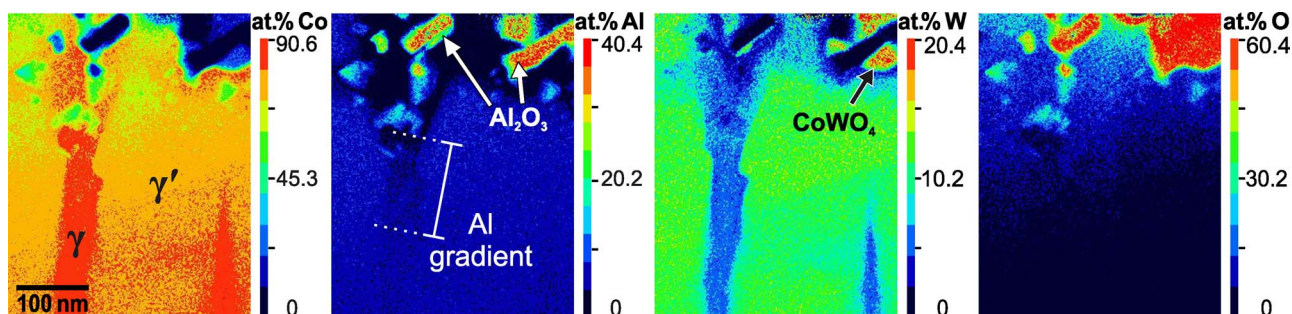

Fig. 8. Colour coded element distribution maps (in at.%) for, Co, Al, W and O (left to right) showing the same area around the IOF after 5 min exposure. The two-phase (γ / γ′) microstructure is revealed on the bottom of each map and marked in the Co map.
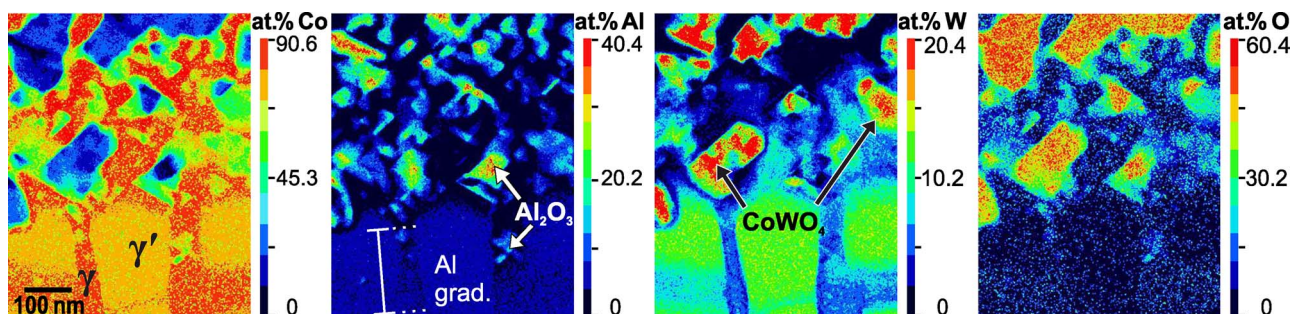
Fig. 9. Colour coded element distribution maps (in at.%) for, Co, Al, W and O (left to right) showing the same area around the IOF after 30 min exposure. The two-phase (γ / γ′) microstructure is revealed on the bottom of each map and marked in the Co map.

duration of oxidation, the flux of oxygen at the IOF continuously decreases. In contrast, prior to the establishment of an extensive Al-depleted zone, the Al flux from the alloy can be assumed to remain nearly constant. In the progress of scale formation, the balance between the described fluxes changes to a favoured formation of larger Al_2O_3 precipitates. As described by several authors, the appearance of such precipitates is mainly determined by the progress of oxidation as well as the nucleation and growth rate of Al_2O_3 in the alloy. Referring to the work of Zhao et al. [28], a high number of discrete precipitates seen in the STEM-EDX mappings of the region enclosing the IOF (Figs. 8–10) indicates a high nucleation rate of Al_2O_3 in the matrix. Furthermore, the morphology of Al_2O_3 precipitates seen at the IOF after 5 h still speaks for a state of relatively fast internal oxidation. These findings correspond nicely with the kinetic investigations from the first part of this work, comparing the time dependency of the instantaneous time exponent (Fig. 1b) and the appearance of the internal precipitation regions after 12 h of oxidation. Combination of all results leads to the conclusion that an almost steady-state of scale formation is reached after 12 h oxidation. Subsequently the two-phase structure finally loses its importance.

4.2. Elemental fluxes in the internal oxidation front

Fig. 11 is a schematic summary of the time-dependent transformations in a constant volume increment surrounding the IOF. The first two images were chosen to describe the situation during the fast internal progress between initiation stage and 30 min oxidation. Supply of Al proceeds solely from the γ phase. The gradient of Al concentration along the channels (compare Figs. 8 and 9) offers the striking proof for this hypothesis. Since no Al partitioning preference could be found in ternary Co-base superalloys [31], our finding regarding the Al depletion which only expands along the γ channel is even more outstanding. Stronger binding of Al in the intermetallic γ′ phase might further hinder the diffusion of Al from the precipitate into the channel. For longer durations the gradient indicating Al depletion spreads further into the alloy.

Initiation of an γ′ depleted zone can be seen after 5 h of oxidation

(compare Fig. 9) and is schematically shown in t_3 (Fig. 11). At this stage, the flux of Al comes from both phases, accompanied by the onset of γ′ dissolution. At t_4 which represents a stage between 5 and 12 h, stronger depletion of Al leads to the formation of unfavourable needle like Co_3W structures in the internal precipitation region. After 12 h the progress of oxidation is in a quasi-steady-state, where the decrease of oxygen flux at the IOF leads to coarsening of the formed oxides, without changing diffusion velocities significantly. These findings correspond nicely to the n^{inst}-t curve from Fig. 1. The SEM micrographs of the scale after 72 and 100 h show small regions covered by dark Al_2O_3-islands (Fig. 3). Even though an Al_2O_3 layer is known to be one of the most effective diffusion barriers, its growth rate in lateral direction might be relatively fast, considering the substantial overall thickness of the scale, and therefore its growth considerably contributes to the overall mass gain. The slight increase of n^{inst} after 70 h of oxidation may be due to the more favourable balance of mass flows which then lead to the lateral growth of protective Al_2O_3 partially spreading over the sample. The significant growth of protective oxide might have faster kinetics and could in turn slightly increase the slope of the mass gain curve.

4.3. Scale composition during quasi-steady-state oxidation

The schematic drawing in Fig. 12 summarises the experimental findings by showing a cut through the scale focusing on the layering, especially in the inner oxide layer. The situation shown in the schematic diagram represents the quasi-steady-state which is established between 12 and 24 h of oxidation at 900 °C. Directly below the interface between d_1 and d_2, a narrow oxidised region, displaying a morphology comparable to the original two-phase microstructure can still be recognised. Due to the location it is reasonable to assume that these structures were formed during the early stages of scale formation. As demonstrated by the elemental distribution maps of samples oxidised for 5 and 30 min (Figs. 7–9), large quantities of Al from the γ phase are instantly consumed by the formation of Al_2O_3 on the IOF. After short exposure times, $CoWO_4$ was found in close proximity of Al_2O_3 in the γ channels at the IOF. During the ongoing oxidation process, a second oxidation front advances into the alloy. Right below the original alloy surface, only the
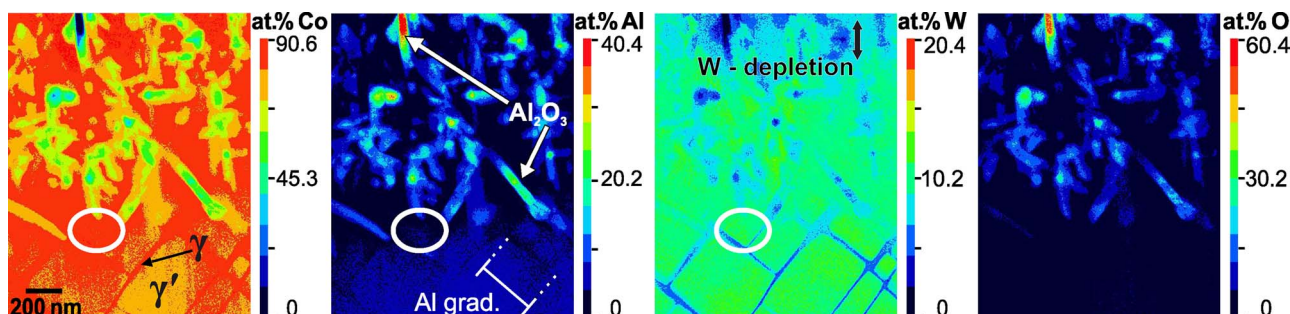

Fig. 10. Colour coded element distribution maps (in at.%) for, Co, Al, W and O (left to right) showing the same area around the IOF after 5 h exposure. The two-phase (γ / γ′) microstructure is revealed on the bottom of each map and marked in the Co map.
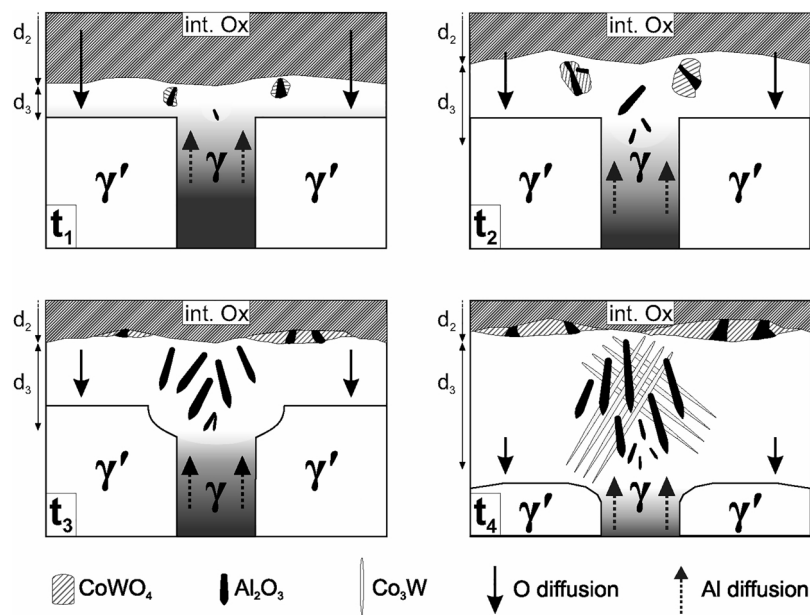
Fig. 11. Schematic diagram, highlighting the structural changes on the IOF. Shown are four different durations of exposure ($t_1 < t_2 < t_3 < t_4$). For simplicity, besides the diffusion of oxygen only the diffusion and depletion (gradient in γ-channel) of Al is taken into account.
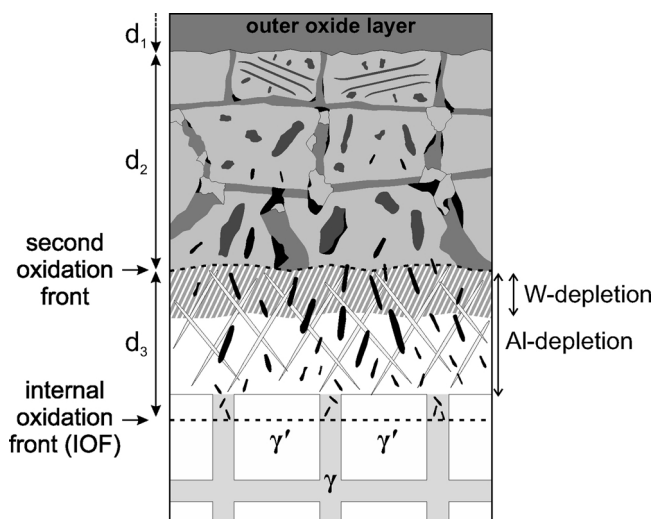

Fig. 12. Schematic representation of a multilayered scale grown on ternary Co-base superalloys after oxidation at 900 °C for a duration t ($t > t_4$). The focus is set on the developed oxidation fronts. Different gray values are used for distinct oxides, imitating *Z*-contrast seen in Fig. 6 as well as particular morphological features.

γ channels were oxidised due to fast internal oxidation during the first minutes of exposure. Since Al is still present in regions formerly covered by γ′ cubes, additional Al containing oxides have to be formed there. One deliberately chosen part of the aforementioned area is magnified in Fig. 6 and clearly shows lamellar $CoAl_2O_4$ spinels embedded in $CoWO_4$. The distinctive structure in this narrow region is observed in all investigated scales unaffected by the exposure time.

Besides the obvious and sufficiently discussed Al-depletion, another region depleted also in W was measured by STEM-EDX. In the foregoing, the diffusion behaviour of W was hardly discussed. From recent literature studies on diffusion of alloying elements in binary Co-X alloys, it can be concluded that W diffusion is orders of magnitude slower than Al diffusion in ternary Co-base superalloys [32–34]. Nevertheless, after Al is completely consumed, the next stable of the found oxide phases is $CoWO_4$. With steadily decreasing propagation velocity of the identified second oxidation front, also the content of the slower

diffusing W visibly declines. Depletion of W can be seen in the BSE images of the cross-sections for oxidation times longer than 5 h, as darker seam formed right below the interface of d_2 and d_3 (compare Fig. 3). Besides the overall concentration of W in the alloy, the slow diffusion velocity leads to a negligible role of this element in the formation of protective Al_2O_3 layers.

With all results presented so far, the absence of a closed Al_2O_3 layer after the first 100 h oxidation at 900 °C of the investigated ternary superalloy becomes explainable. Most detrimental for the formation of this protective layer are the fast progress of internal oxidation and high nucleation rates of Al_2O_3. Even though diffusion through the outer oxide layer was not in the focus of this work, a high defect density in the outer CoO layer, combined with porosity, classically reported for conventional Co-Al-(Cr) alloys (e.g. [35,36]) also leads to fast progress of the IOF and therefore to formation of relatively small Al_2O_3 precipitates in ternary Co-base superalloys. Diffusion follows an Arrhenius dependency with temperature. Changes of temperature might affect the relevant elemental fluxes, diffusion of O and Al towards the IOF to a different extent. This could be the explanation, why the growth of an Al_2O_3 layer in contrast to Ni-base superalloys is favourable at lower temperatures. A similar relationship was already described by Irvine for binary Co-Al alloys revealing even higher Al-contents, between 14 and 19 at.%. The observation that the oxide morphologies at the IOF are quite comparable between binary Co-Al alloys and ternary γ′-strengthened ternary superalloys supports the conclusion that the given W-content plays a minor influence during the formation of new oxides in the early, transient periods of oxidation. Nevertheless, for longer oxidation times, higher W-contents might significantly alter diffusion velocities of both O and Al within the alloy. If the progress of the IOF is more significantly suppressed, the probability of lateral Al_2O_3 growth increases, also for higher temperature regimes. The influence of W-content at constant Al concentration as well as diffusion through the outer oxide layer will therefore be topics for supplementary studies to provide as complete an understanding of the elementary oxidation mechanisms of ternary Co-base superalloys as possible.

The present paper reveals until now unseen differences between matrix and hardening phase during the early stages of oxidation. In view of protective oxide formation, triggering the dimension of the two-phase microstructure by heat treatment alone will not lead to formation of a protective alumina layer. Rather, widening the tolerance of Al in

the two-phase region by alloying with further elements can be a challenge for future alloy development. High Al concentration in the γ phase can be a key point, since this work showed that oxidation of ternary Co-base superalloys during the first hours is mainly driven by diffusion inside the matrix phase. Another positive aspect of a widened two-phase field might be the later formation of undesired ternary phases such as Co_3W.

5. Conclusions

A detailed study on the oxidation behaviour of a single crystal ternary Co-base superalloy including the transient stages of oxidation was presented. Thermogravimetric analysis combined with high-resolution STEM-EDX lead to the following conclusions:

1. An overall parabolic growth kinetic for the three individual oxide layers could be confirmed. Parabolic rate constants of each layer strongly depend on the progress of oxidation and were calculated.
2. Al_2O_3 starts to nucleate in the γ channels. STEM-EDX was used to demonstrate the existence of finely dispersed CoO, $CoWO_4$ and $CoAl_2O_4$ in the inner oxidation zone. High-resolution elemental mappings confirmed the influence of the former two-phase microstructure on the appearance of the inner oxidation zone.
3. Propagation of the IOF takes place solely along the γ phase. The existence of a second propagating oxidation front was demonstrated.
4. Clear conclusions on the diffusion of alloying elements were drawn: During the first hours after initiation of internal scale formation, Al is exclusively provided by the γ channels.
   After 5 h of oxidation also Al from the γ' phase starts to diffuse to the internal oxidation front.
   A quasi-steady-state in the oxidation kinetics is reached for exposure times longer than 12 h.
5. Due to the disadvantageous ratio of elemental fluxes to the IOF combined with the high nucleation rate of Al_2O_3 precipitates, no protective Al_2O_3 layer is formed during 100 h isothermal oxidation at 900 °C.

Acknowledgments

References

[1] J. Sato, T. Omori, K. Oikawa, I. Ohnuma, R. Kainuma, K. Ishida, Cobalt-base high-temperature alloys, Science 312 (2006) 90–91.
[2] R. Reed, The Superalloys Fundamentals and Applications, Cambridge University Press, 2006.
[3] K. Shinagawa, T. Omori, J. Sato, K. Oikawa, I. Ohnuma, R. Kainuma, K. Ishida, Phase equilibria and microstructure on γ' phase in Co-Ni-Al-W system, Mater. Trans. 49 (2008) 1474–1479.
[4] A. Suzuki, T. Pollock, High-temperature strength and deformation of γ/γ' two-phase Co-Al-W-base alloys, Acta Mater. 56 (2008) 1288–1297.
[5] A. Bauer, S. Neumeier, F. Pyczak, M. Göken, Microstructure and creep strength of different γ/γ'-strengthened Co-base superalloy variants, Scr. Mater. 63 (2010) 1197–1200.
[6] A. Bauer, S. Neumeier, F. Pyczak, R. Singer, M. Göken, Creep properties of different γ'-strengthened Co-base superalloys, Mater. Sci. Eng. A 550 (2012) 333–341.
[7] T. Pollock, J. Dibbern, M. Tsunekane, J. Zhu, A. Suzuki, New Co-based γ–γ' high-temperature alloys, JOM 62 (2010) 58–63.
[8] L. Klein, Y. Shen, M. Killian, S. Virtanen, Effect of B and Cr on the high temperature oxidation behaviour of novel γ/γ'-strengthened Co-base superalloys, Corros. Sci. 53 (2011) 2713–2720.
[9] L. Klein, A. Bauer, S. Neumeier, M. Göken, S. Virtanen, High temperature oxidation of γ/γ'-strengthened Co-base superalloys, Corros. Sci. 53 (2011) 2027–2034.
[10] L. Klein, M. Killian, S. Virtanen, The effect of nickel and silicon addition on some oxidation properties of novel Co-based high temperature alloys, Corros. Sci. 69 (2012) 43–49.
[11] H.-Y. Yan, V. Vorontsov, D. Dye, Effect of alloying on the oxidation behaviour of Co-Al-W superalloys, Corros. Sci. 83 (2014) 382–395.
[12] C. Stewart, R. Rhein, A. Suzuki, T. Pollock, C. Levi, Oxide scale formation in novel γ/γ' Cobalt-based alloys, Proceedings of the International Symposium on Superalloys 2016 (2016) 991–999.
[13] C. Giggins, F. Pettit, Oxidation of Ni-Cr-Al alloys between 1000 and 1200 ° C, J. Electrochem. Soc. 118 (1971) 1782–1790.
[14] R. Prescott, M. Graham, The formation of aluminum oxide scales on high-temperature alloys, Oxid. Met. 38 (1992) 233–254.
[15] I. Edmonds, H. Evans, C. Jones, R. Broomfield, Intermediate temperature internal oxidation in fourth generation Ru-bearing Single-crystal nickel-base superalloys, Oxid. Met. 69 (2008) 95–108.
[16] I. Edmonds, H. Evans, C. Jones, The role of the γ' precipitate dispersion in forming a protective scale on ni-based superalloys at 750 °C, Oxid. Met. 73 (2010) 193–206.
[17] Q. Ding, Z. Shen, S. Xiang, H. Tian, J. Li, Z. Zhang, In-situ environmental TEM study of γ'/γ-phase transformation induced by oxidation in a nickel-based single crystal superalloy, J. Alloys Compd. 651 (2015) 255–258.
[18] J. Yang, K. Nadarzinski, E. Schumann, M. Rühle, Electron microscopy studies of NiAl/γ-Al$_2$O$_3$ interfaces, Scr. Metall. Mater. 33 (1995) 1043–1048.
[19] F. Liu, H. Götlind, J.-E. Svensson, L.-G. Johansson, M. Halvarsson, Early stages of the oxidation of a FeCrAlRE alloy (Kanthal AF) at 900 °C: a detailed microstructural investigation, Corros. Sci. 50 (2008) 2272–2281.
[20] A. D'Alfonso, B. Freitag, D. Klenov, L. Allen, Atomic-resolution chemical mapping using energy-dispersive X-ray spectroscopy, Phys. Rev. B Condens. Matter Mater. Phys. 81 (2010) 103–111.
[21] L. Allen, A. D'Alfonso, B. Freitag, D. Klenov, Chemical mapping at atomic resolution using energy-dispersive X-ray spectroscopy, MRS Bull. 37 (2012) 47–52.
[22] M.-W. Chu, S. Liou, C.-P. Chang, F.-S. Choa, C. Chen, Emergent chemical mapping at atomic-column resolution by energy-dispersive X-ray spectroscopy in an aberration-corrected electron microscope, Phys. Rev. Lett. 104 (2010) 196101.
[23] W. Zhao, Z. Li, B. Gleeson, A new kinetics-based approach to quantifying the extent of metastable → stable phase transformation in thermally-grown Al$_2$O$_3$ scales, Oxid. Met. 79 (2013) 361–381.
[24] S. Mrowec, On the mechanism of high temperature oxidation of metals and alloys, Corros. Sci. 7 (1967) 563–578.
[25] P. Kofstad, A. Hed, High temperature oxidation of Co-10 w/o Cr alloys, J. Electrochem. Soc. 116 (1969) 224–234.
[26] P. Kofstad, On the formation of porosity and microchannels in growing scales, Oxid. Met. 24 (1985) 265–276.
[27] B. Pieraggi, Calculations of parabolic reaction rate constants, Oxid. Met. 27 (1987) 177–185.
[28] W. Zhao, Y. Kang, J. Orozco, B. Gleeson, Quantitative approach for determining the critical volume fraction for the transition from internal to external oxidation, Oxid. Met. 83 (2015) 187–201.
[29] L. Klein, A. Zendegani, M. Palumbo, S. Fries, S. Virtanen, First approach for thermodynamic modelling of the high temperature oxidation behaviour of ternary γ'-strengthened Co-Al-W superalloys, Corros. Sci. 89 (2014) 1–5.
[30] C. Wagner, Reaktionstypen bei der Oxydation von Legierungen, Zeitschrift für Elektrochemie, Berichte der Bunsengesellschaft für physikalische Chemie 63 (1959) 772–782.
[31] I. Povstugar, P.-P. Choi, S. Neumeier, A. Bauer, C. Zenk, M. Göken, D. Raabe, Elemental partitioning and mechanical properties of Ti- and Ta-containing Co-Al-W-base superalloys studied by atom probe tomography and nanoindentation, Acta Mater. 78 (2014) 78–85.
[32] Y.-W. Cui, B. Tang, R. Kato, R. Kainuma, K. Ishida, Interdiffusion and atomic mobility for face-centered-cubic Co-Al alloys, Metall. Mater. Trans. A: Phys. Metall. Mater. Sci. 42 (2011) 2542–2546.
[33] Y.-W. Cui, G. Xu, R. Kato, X.-G. Lu, R. Kainuma, K. Ishida, Interdiffusion and atomic mobility for face-centered cubic (fcc) Co-W alloys, Metall. Mater. Trans. A: Phys. Metall. Mater. Sci. 44 (2013) 1621–1625.
[34] S. Neumeier, H. Rehman, J. Neuner, C. Zenk, S. Michel, S. Schuwalow, J. Rogal, R. Drautz, M. Göken, Diffusion of solutes in fcc cobalt investigated by diffusion couples and first principles kinetic Monte Carlo, Acta Mater. 106 (2016) 304–312.
[35] G. Irving, J. Stringer, D. Whittle, The high-temperature oxidation resistance of Co-Al alloys, Oxid. Met. 9 (1975) 427–440.
[36] J. Smeggil, A. Shuskus, J. Smeggil, A. Shuskus, The oxidation behavior of CoCrAlY, CoCrAl and yttrium-implanted CoCrAl alloys compared and contrasted, Surf. Coat. Technol. 32 (1987) 57–68.